Unified view of avalanche criticality in sheared glasses

Norihiro Oyama,[1,2,*] Hideyuki Mizuno,[1] and Atsushi Ikeda[1,3]

[1]*Graduate School of Arts and Sciences, The University of Tokyo, Komaba, Tokyo 153-8902, Japan*

[2]*Mathematics for Advanced Materials-OIL, AIST, Sendai 980-8577, Japan*

[3]*Research Center for Complex Systems Biology, Universal Biology Institute, The University of Tokyo, Komaba, Tokyo 153-8902, Japan*

(Received 16 September 2020; revised 21 March 2021; accepted 14 June 2021; published 12 July 2021)

Plastic events in sheared glasses are considered an example of so-called avalanches, whose sizes obey a power-law probability distribution with the avalanche critical exponent τ. Although the so-called mean-field depinning (MFD) theory predicts a universal value of this exponent, $\tau_{\mathrm{MFD}} = 1.5$, such a simplification is now known to connote qualitative disagreement with realistic systems. Numerically and experimentally, different values of τ have been reported depending on the literature. Moreover, in the elastic regime, it has been noted that the critical exponent can be different from that in the steady state, and even criticality itself is a matter of debate. Because these confusingly varying results have been reported under different setups, our knowledge of avalanche criticality in sheared glasses is greatly limited. To gain a unified understanding, in this work, we conduct a comprehensive numerical investigation of avalanches in Lennard-Jones glasses under athermal quasistatic shear. In particular, by excluding the ambiguity and arbitrariness that has crept into the conventional measurement schemes, we achieve high-precision measurement and demonstrate that the exponent τ in the steady state follows the prediction of MFD theory, $\tau_{\mathrm{MFD}} = 1.5$. Our results also suggest that there are two qualitatively different avalanche events. This binariness leads to the nonuniversal behavior of the avalanche size distribution and is likely to be the cause of the varying values of τ reported thus far. To investigate the dependence of criticality and universality on applied shear, we further study the statistics of avalanches in the elastic regime and the ensemble of the first avalanche event in different samples, which provide information about the unperturbed system. We show that while the unperturbed system is indeed off-critical, criticality gradually develops as shear is applied. The degree of criticality is encoded in the fractal dimension of the avalanches, which starts from zero in the off-critical unperturbed state and saturates in the steady state. Moreover, the critical exponent τ is consistent with the prediction of the MFD τ_{MFD} universally, regardless of the amount of applied shear, once the system becomes critical.

DOI: 10.1103/PhysRevE.104.015002

I. INTRODUCTION

It has been empirically accepted that various nonequilibrium systems exhibit intermittent fluctuations whose sizes obey a power-law distribution, $P(S) \sim S^{-\tau}$, where S is an appropriately defined size of intermittent events and $\tau > 0$ is the critical exponent. Such intermittent and scale-free fluctuations are called avalanches, and the nature of the criticality of these fluctuations is expected to form (sub-)classes of nonequilibrium universality [1]. Possible candidates for members of these classes cover a very wide range, including snow avalanches [2] (as the name suggests), Barkhausen noise [3,4], the depinning transition of elastic bodies moving in random media [5,6], charge excitations in electron glasses [7], microcrystal collapse under external forces [8], earthquakes [9,10], the flickering of faraway stars [11], the extinction of biological species [12], the firings of neuronal networks [13,14], and decision-making processes [15]. Note that the theories of some of these examples provide the same value of the critical exponent $\tau = 1.5$, at least at the mean-field level [3,6,8,10]

Glasses under external fields such as shearing deformation or compression, the target system of this article, have also been found to exhibit intermittent noise [16–25]. In the case of sheared amorphous solids, the intermittency comes from plastic events. The elementary process of plastic events is believed to be so-called local shear transformation zones (STZs), which are triggered when the lowest eigenvalue of the dynamical matrix becomes zero [16,26]. STZs interact with each other via an elastic field, so the energy released from an excited STZ can trigger further excitation of others [27]. Such a chain of STZs leads to scale-free avalanches. The theoretical treatment of avalanches in sheared amorphous solids has been achieved in mean-field depinning (MFD) theory [28,29], and it has been shown that the critical exponent coincides with the universal value $\tau_{\mathrm{MFD}} = 1.5$ reported for other systems, such as Barkhausen noise [3], the depinning transition of elastic bodies moving in random media [6], plastic events in deformed crystals [8], and earthquakes [10]. However, we note that it has recently been shown that the simplification employed in this MFD approach [8] connotes several qualitative disagreements with realistic systems. Specifically, although the elastic interaction kernels between STZs are assumed to be *monotonic* [6] in the MFD model [8], they are known

*oyamanorihiro@g.ecc.u-tokyo.ac.jp

to be *nonmonotonic* (quadrupolar shapes) [30] in sheared glasses. This qualitative difference results in a failure of a correct prediction for an important scaling behavior: while the average value of the strain interval between avalanches $\langle \delta\gamma \rangle$ is known to scale with the system size N as $\langle \delta\gamma \rangle \sim N^{-\chi}$ with $0 < \chi < 1$ [31–34], the monotonic kernel employed in Ref. [8] leads to trivially $\langle \delta\gamma \rangle \sim 1/N$ [33]. Notice that several recent mean-field treatments succeeded in reproducing this subextensive nature [35–37] (see Appendix F for the summary of values of exponents that have been reported in recent previous works).

Many experimental and numerical studies have also been carried out. Experimentally, although there are still variations in the precise value of τ depending on the literature [38,39], it has recently been reported that the values of τ in various systems are universally close to the MFD prediction $\tau_{\mathrm{MFD}} = 1.5$ [40–44]. In particular, since the precise value of τ is sensitive to the temporal resolution of the measurement [45] and a study using a high resolution [40] has reported a value of τ consistent with τ_{MFD}, a consensus is being established—that the critical exponent in real systems universally follows the prediction of the MFD model [8]. We stress again that this result is surprising, considering the qualitative disagreement with the real systems that MFD theory involves.

For many situations, numerical simulations can serve as powerful tools that allow us to perform precisely controlled idealized *numerical experiments*. In particular, simulations under an idealized condition have been performed to study avalanches in sheared amorphous solids: in most numerical works, the limit of zero temperature and zero strain rate, so-called athermal quasistatic (AQS) shear, is employed [46]. Many studies have reported measurement results of τ under AQS shear with various setups that have included different frameworks—namely, atomistic simulations [39,47–52] and elastoplastic models [34,53–57]. Some of these works further conducted finite-size scaling to validate the obtained value of τ. However, the value of τ varies greatly from study to study in the range of 1.0 to 1.36 [34,39,47–58][1] (if we restrict the targets to only recent atomistic simulations, the range becomes $\tau \in [1.0, 1.3]$ [47–49,52]).[2] Note that such variation is found even within the same numerical framework. In other words, even with the aid of idealized numerical experiments, thus far, we have obtained only system-dependent values of critical exponents, and no clues of consistency with $\tau_{\mathrm{MFD}} = 1.5$ have been found. This situation is at odds with that of experimental studies where multiple works have reported $\tau \approx \tau_{\mathrm{MFD}}$.

Furthermore, theoretically and numerically, a new view has been proposed recently, making the situation even more confusing. The new view states that avalanches in the elastic regime exhibit very different statistics than those in a steady state: a mean-field replica theory specific to the elastic regime [60] predicts that the critical exponent in this regime should be $\tau_{\mathrm{R}} = 1.0$ (if the system is *above jamming*), and a recent numerical work [52] has reported consistent results in a binary Lennard-Jones (LJ) glass system. The value of $\tau_{\mathrm{R}} = 1.0$ is markedly smaller than the values reported in the steady state, $\tau \in [1.15, 1.3]$ [47–49], so the possibility of a change in the universality class after the yielding transition takes place has been suggested [52]. However, even if we look at similar strain regimes, different values ($\tau = 1.1, 1.2$) that are consistent with the results in the steady state have been reported in other numerical works under AQS shear [50,61]. Additionally, we highlight that experiments with high temporal resolution [40] reporting $\tau \approx \tau_{\mathrm{MFD}} = 1.5$ were conducted in the elastic regime. Therefore, the value of the critical exponent in the elastic regime is still under debate as well. Moreover, Ref. [32] reported that, in the first place, the systems do not exhibit criticality in the limit of $\gamma \to 0$, where γ is the accumulated applied shear strain. Since all these seemingly conflicting results have been reported under various numerical setups, we still lack a firm understanding with a unified perspective.

In this work, to resolve this puzzling situation concerning avalanche criticality and universality presented above and to provide a unified view, we investigate the statistics of avalanches in sheared glasses comprehensively by means of atomistic simulations of binary LJ glasses under AQS simple shear. First, by excluding the ambiguity and arbitrariness that unexpectedly crept into the measurement of avalanche statistics in previous works, we show that the critical exponent τ in the steady state coincides with the universal value obtained by MFD theory in Ref. [8], $\tau_{\mathrm{MFD}} = 1.5$. We stress that we obtain this value using scaling relations, not by direct fitting of the data, which would require choosing the fitting range, thereby introducing unintentional arbitrariness. Our results also suggest that the scaling function of the avalanche size distribution has a peculiar bump and thus is different from standard cases, such as exponential cutoffs. We find that there are two qualitatively different avalanche events, which we call precursors and mainshocks. Precursors and mainshocks follow different probability distribution functions (PDFs), and the peculiar bump of the scaling function is found to be due only to the contributions from mainshocks; these include system-spanning events and suffer from the finite-size effect. Importantly, we also demonstrate that this bumpiness in the scaling function explains the nonuniversal values of τ reported in previous studies.

We then perform the same high-precision measurement in the elastic regime to investigate whether we indeed observe shear-dependent changes in criticality and universality. In particular, we separately measure the statistics of both the ensembles of only the initial avalanche events of different samples, which reflect the property of the unperturbed system ($\gamma \to 0$), and the avalanches collected in the elastic regime $0 \leqslant \gamma \leqslant 0.02$ [52]. The former case does not exhibit any system size dependence, in accordance with Ref. [32]. Meanwhile, the latter case does show system size dependence, or criticality, in agreement with Refs. [52,62]. This criticality in the elastic regime is clearly different from that in the steady state and is characterized by a much smaller fractal dimension. Nevertheless, consistent with the experimental results [40,42], the value of $\tau \approx 1.505$ estimated by the scaling relation is very close to the steady-state value and τ_{MFD}. All these results

[1]The maximum value becomes 1.5 if we also include systems under oscillatory shear [29,59].

[2]Here only works with finite-size scalings are considered. Before these works, much smaller values were reported, such as in Ref. [16]. Additionally, Refs. [39] and [51] reported larger values.

provide a unified view of avalanche criticality in sheared LJ glasses: criticality develops as shear is exerted, and the critical exponent τ remains the same universally once the system becomes critical. The development of criticality is reflected by the increasing value of the fractal dimension, from zero in the off-critical unperturbed system to a saturated value in the steady state.

This article is organized as follows: In Sec. II the numerical methods are summarized. In particular, we introduce a new measurement scheme and important scaling relations, including recapitulating those proposed in Ref. [34]. The results for the steady state are presented in Sec. III. In Sec. IV the results of the elastic regime are presented, and the unified view of avalanche criticality and universality throughout the whole strain regime is provided. Finally, concluding remarks are presented in Sec. V.

II. METHODS

In this work, we conduct simulations of two-dimensional ($d = 2$) sheared binary LJ glasses and investigate the avalanche statistics in detail. Specifically, we aim to exclude ambiguities from the definition and measurement of avalanche sizes. In this section, we first explain the numerical setup of our binary LJ glass system under AQS shear in Sec. II A. In Sec. II B we propose a brand-new measurement scheme for avalanches. In the subsequent section, Sec. II C, we discuss the importance of system size-dependent tuning of the numerical strain interval $\Delta\gamma$, which has not been taken seriously thus far. Finally, the scaling relations proposed in Ref. [34] are summarized in Sec. II D in a way that is compatible with our setup.

A. Target system

For the interparticle potential, we employ the smoothed LJ potential [48], defined as

$$\phi_{\rm L}(r_{ij}) = 4\epsilon_{ij}\left[\left(\frac{d_{ij}}{r_{ij}}\right)^{12} - \left(\frac{d_{ij}}{r_{ij}}\right)^{6}\right] + \epsilon_{\rm C} \quad (r_{ij} < I_{ij}), \quad (1)$$

$$\phi_{\rm R}(r_{ij}) = \frac{C_3}{3}\left(r_{ij} - r_{ij}^{\rm C}\right)^3 + \frac{C_4}{4}\left(r_{ij} - r_{ij}^{\rm C}\right)^4 \quad \left(I_{ij} \leqslant r_{ij} < r_{ij}^{\rm C}\right), \quad (2)$$

where r_{ij} is the interparticle distance between particles i and j, d_{ij} determines the interaction range, and $\epsilon_{\rm C}$ is the potential offset, which guarantees that $\phi_{\rm L}$ and $\phi_{\rm R}$ (and their first and second derivatives) match at the inner cutoff $I_{ij} \equiv 1.2d_{ij}$. The coefficients C_3 and C_4 are chosen so that $\phi_{\rm R}$ and its first and second derivatives continuously go to zero at the outer cutoff $r_{ij}^{\rm C} \equiv 1.3d_{ij}$. To avoid crystallization, the system is composed of two different sizes of particles, species S and L, at a ratio of 50:50. The potential is totally additive, and the interaction ranges are $d_{\rm SS} = 5/6$, $d_{\rm SL} = 1.0$ and $d_{\rm LL} = 7/6$, respectively. The energy unit $\epsilon_{ij} = \epsilon = 1.0$ is constant for all combinations of particle species. Below, all physical variables are nondimensionalized by the length unit d_{SL} and the energy unit ϵ. The number density of the system is fixed at $\rho = N/L^2 \approx 1.09$. All samples are generated by minimizing the potential energy of a completely random initial configuration, which corresponds to an infinite temperature.

The system is driven out of equilibrium by external simple shear. The simple shear is imposed on the whole system in a quasistatic way without any thermal noise. This protocol is called AQS shear and is achieved by the repetition of very tiny affine shearing deformations of the strain increment $\Delta\gamma$, followed by energy minimization under the Lees-Edwards boundary condition [63]. The energy is considered to be minimized when the maximum magnitude of the forces applied to the particles $f_{\rm max}$ meets the condition $f_{\rm max} < 10^{-9}$. We use the FIRE (Fast Inertial Relaxation Engine) algorithm for energy minimization [64]. The distinguishing feature of this FIRE algorithm from other major energy minimization protocols, e.g., the conjugate gradient (CG) method, is the presence of the inertia in the dynamics during the energy minimization. It is widely accepted that such an inclusion of the inertia improves the speed of the convergence of the energy minimization compared to the CG method in many problems. Although several works have reported that the introduction of inertia during energy minimization can affect the avalanche statistics, such an effect seems to be absent from our results (see Appendix C). Even under these conditions, we still have one free parameter—namely, the strain resolution per numerical step $\Delta\gamma$. In this work, we tune this parameter depending on the system size N, and this tuning plays a fundamental role in measuring the avalanche exponent τ. The determination of $\Delta\gamma$ will be discussed in Sec. II C.

B. Rewinding method and the definition of avalanches

To evaluate the sizes of avalanches that are purely due to plastic events, stress drops (or potential energy drops) should be measured under the same boundary conditions. For this reason, in previous studies [19,49,50,52], the size of the ith avalanche S_i is defined as the sum of the stress drop and linear correction, as

$$S_i \equiv L^d(\Delta\sigma_i + G\Delta\gamma), \quad (3)$$

where $\Delta\sigma_i \equiv \sigma(\gamma_{Ci}) - \sigma(\gamma_{Ci} + \Delta\gamma)$ is the stress drop during the ith avalanche, γ_{Ci} is the critical strain at which the ith avalanche takes place, and G is the shear modulus (Fig. 1). However, as discussed in Ref. [16], the value of the shear modulus G fluctuates strongly when an external shear is applied. In particular, G becomes infinite in the negative direction at the onset of an avalanche, where the lowest eigenvalue of the dynamical matrix becomes zero. It is even possible that a single stress drop event can take several numerical strain steps when the strain resolution $\Delta\gamma$ is very fine [16]. Therefore, it is quite nontrivial to determine which kind of definition of the modulus should be used for the linear correction in Eq. (3) and how different definitions affect the results.

To rule out such an ambiguity in the definition of avalanche sizes, we developed a new measurement scheme: when a stress drop event is detected, we reverse the direction of shear and rewind the strain by one strain step $\Delta\gamma$ (see Fig. 1). We call this scheme *the rewinding method*. From the perspective of the potential energy landscape picture, a plastic event can be viewed as a transition from one metabasin to another: states A (original) and B (new). The rewinding method enables us to directly compare the variables of these two states A and B at exactly the same boundary condition $\gamma = \gamma_{Ci}$. Thus, we

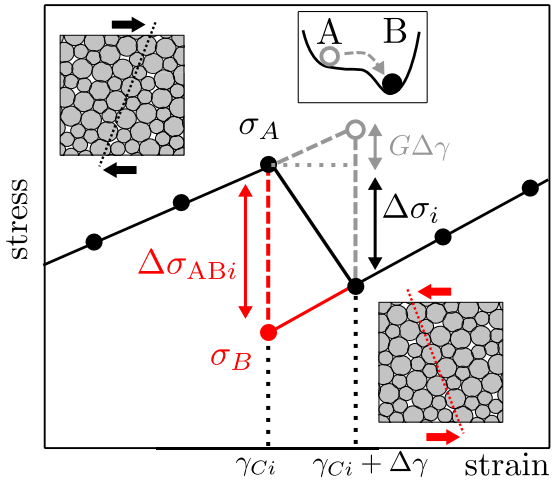

FIG. 1. Schematic of the rewinding method. The black lines and points represent the results of a normal AQS simulation. The gray lines and points depict the conventional definition of the avalanche size with a linear correction. The red lines and points represent our definition of the avalanche size using the rewinding method.

can define the ith avalanche size S_i simply by the difference between the stresses of the two states without any ambiguity, as

$$S_i = L^d \Delta\sigma_{ABi}, \tag{4}$$

where $\Delta\sigma_{ABi} \equiv \sigma_A(\gamma_{Ci}) - \sigma_B(\gamma_{Ci})$ and $\sigma_s(\gamma)$ denotes the stress of state $s \in A, B$ at strain γ. Hereafter, all our analyses are based on this definition, Eq. (4) (see Appendix G for comparison with the conventional linear correction method). We emphasize that we do not introduce any lower cutoff size for avalanche detection [50,52], and we utilize all stress drop events in this work.

C. Strain resolution

Since the average of the strain intervals between avalanches, $\delta\gamma_i \equiv \gamma_{Ci+1} - \gamma_{Ci}$, is known to decrease with increasing system size N as $\langle\delta\gamma\rangle \sim N^{-\chi}$ with a positive exponent $0 < \chi < 1$ [31,32,34], larger systems require finer strain resolutions to detect small avalanches properly. In other words, if we do not care about the strain resolution $\Delta\gamma$, the statistics of small avalanches in large systems can be obscured. However, thus far, in most cases, $\Delta\gamma$ has been more or less fixed to a single value regardless of the system size. Alternatively, a smallest size cutoff for avalanche detection has sometimes been introduced [50,52]. Such treatments would be justified if the scale-free power-law behavior appeared in the large-size regime of the PDF of avalanche sizes close to the cutoff size S_c. As discussed later, however, our results show that this is not the case and indicate the importance of tuning the strain resolution $\Delta\gamma$ depending on the system size. The precise values of the strain resolution $\Delta\gamma(N)$ that we used for the different system sizes are summarized in Table I. See Appendix D for how we determined these values and how the results are affected if we do not tune $\Delta\gamma$ properly.

TABLE I. Values of strain resolution.

N	512	2048	8192	32 768	131 072[a]
$\Delta\gamma$	5×10^{-6}	5×10^{-6}	5×10^{-6}	1×10^{-6}	5×10^{-7}

[a]For only the first events and the elastic regime.

D. Scaling laws

In this section, we summarize the scaling relation, which reduces the number of independent critical exponents through physical constraints. In particular, by following the original discussion in Ref. [34], we show that these relations are closed by only two exponents. We list all six related critical exponents in Table II, and to ensure that the article is self-contained, we recapitulate the derivations of all the relations.

We introduce two different PDFs of avalanche sizes. The first, $P(S)$, is the standard normalized PDF per unit avalanche size and is simply given as

$$\int P(S)\, dS = 1. \tag{5}$$

The other, $R(S)$, is the PDF per unit avalanche size and unit strain. If we define the average number of avalanche events per unit strain $M(L)$ as

$$M(L) = \int_0^\infty R(S, L)\, dS, \tag{6}$$

then these three functions can be related to each other as

$$P(S, L) = R(S, L)/M(L), \tag{7}$$

where L is the linear dimension of the system. We now explicitly write the system size dependence of the PDFs. In the field of avalanches in sheared glasses [47–49,52], the PDF per unit strain $R(S)$ is usually preferred to the standard PDF $P(S)$.

We now assume the criticality of avalanches and that the distribution has a system size-dependent cutoff size $S_c \sim L^{d_f}$, where d_f is the fractal dimension. Then, by introducing a scaling function $f(S/S_c)$ as $P(S) = S^{-\tau} f(S/S_c)$, we obtain a scaling relation for $P(S)$:

$$P(S) \sim L^{-d_f\tau}(S/L^{d_f})^{-\tau} f(S/L^{d_f}), \tag{8}$$

$$\sim L^{-d_f\tau} g(S/L^{d_f}), \tag{9}$$

where we introduce another function, $g(S/S_c) \equiv (S/S_c)^\tau f(S/S_c)$. If we substitute $M(L) \sim 1/\langle\delta\gamma(L)\rangle \sim N^\chi$ and Eq. (9) into Eq. (7), we obtain

$$R(S) \sim L^{d\chi - d_f\tau} g(S/L^{d_f}). \tag{10}$$

Thus, comparing Eq. (10) with the definition of the exponent β shown in Table II, we obtain the following relation:

$$\beta = d\chi - d_f\tau. \tag{11}$$

Another relation among τ, χ and d_f can be derived from the stationary condition of stress in the steady state. For $1 < \tau < 2$ (which is the case for avalanches in sheared glasses), the average avalanche size can be derived from $P(S) \sim S^{-\tau}$ as

$$\langle S\rangle \sim S_c^{2-\tau} \sim L^{d_f(2-\tau)}. \tag{12}$$

TABLE II. List of the critical exponents.

Exponent	Definition	Estimation in this work	Steady-state value
χ	$\langle\delta\gamma\rangle \sim N^{-\chi}$	Direct fitting	0.738
d_f	$S_c \sim L^{d_f}$	Direct fitting	1.034
τ	$P(S) \sim S^{-\tau}$	$\tau = 2-(1-\chi)d/d_f$	1.493
α	$\langle S\rangle \sim N^{\alpha}$	$\alpha = (2-\tau)d_f/d = 1-\chi$	0.262
β	$R(X,L) = L^{\beta} g(X/L^{d_f})$	$\beta = d\chi - d_f\tau = d - 2d_f$	−0.068

In the steady state, this value of $\langle S\rangle \equiv L^d\langle\Delta\sigma\rangle$ must be consistent with the average increase in the stress between avalanches. Assuming that the average shear modulus $\bar{G}$ does not depend on the system size statistically, this condition leads to

$$\langle S\rangle = L^d \bar{G}\langle\delta\gamma\rangle \sim L^{d(1-\chi)}. \tag{13}$$

From Eqs. (12) and (13), we obtain the relation

$$\tau = 2-(1-\chi)\frac{d}{d_f}, \tag{14}$$

which plays a central role.

Equations (11) and (14) allow us to write β in a simpler way:

$$\beta = d - 2d_f. \tag{15}$$

Comparing Eq. (12) and the definition of the exponent α shown in Table II, and substituting Eq. (14), we can express α as

$$\alpha = (2-\tau)d_f/d = 1-\chi. \tag{16}$$

All these scaling relations ultimately reduce the number of independent exponents to two. Therefore, we must select two independent exponents and describe others using them. We employ d_f and χ in this work. We stress that while we must choose the fitting range to obtain τ by direct fitting to the avalanche size distribution, the relations $S_c \sim L^{d_f}$ and $\langle\delta\gamma\rangle \sim N^{-\chi}$ are valid for the whole data range, and d_f and χ can be measured without any arbitrariness in the choice of the fitting range.

III. STATISTICS OF AVALANCHES IN THE STEADY STATE

In this section, we present the avalanche statistics in the steady state ($\gamma > 0.25$). For all system sizes, we collected more than 5000 events and calculated the statistical information from them.

A. Independent exponents

We start with the measurement of two independent exponents d_f and χ, which determine all other exponents through the scaling relations introduced in Sec. II D. By definition, these two exponents can be measured from the system size dependence of the average strain interval between avalanches $\langle\delta\gamma\rangle$ and the cutoff avalanche size $S_c \equiv \langle S^2\rangle/\langle S\rangle$ [52]. As shown in Fig. 2, both $\langle\delta\gamma\rangle$ and S_c are power-law functions of the system size N, as expected. We note that, as discussed in Appendix D, if we do not tune $\Delta\gamma$ carefully, $\langle\delta\gamma\rangle$ will not be a power-law function. The obtained exponents and the estimation of the other exponents are summarized in Table II. In Fig. 2(b) we also show the results for $\langle S\rangle$, which yields the exponent α. We note that the direct measurement result $\alpha = 0.269$ shows very close agreement with the estimation by Eq. (16), $\alpha \approx 0.262$. This supports the accuracy of the calculations and the scaling relation. It is also important to mention that the value of $\chi = 0.738$ obtained here is markedly larger than the values in theoretical [32] and other existing numerical works [20,31,32,34,37,47,48,56,57]. See the discussion in Appendix E for detailed comparison with those previous works.

From Eq. (14) and the values of d_f and χ, the avalanche exponent is estimated as $\tau \approx 1.493 \pm 0.041$. We would like to emphasize that this value is very close to a universal value of $\tau_{\mathrm{MFD}} = 1.5$. We also note that this result is surprising because, as presented in the introduction, the applicability of the approximation in the MFD model [8] is recently under discussion [33,57]. To strictly confirm that our result for τ is the intrinsic critical exponent of the system, we conduct further validation in the next two sections.

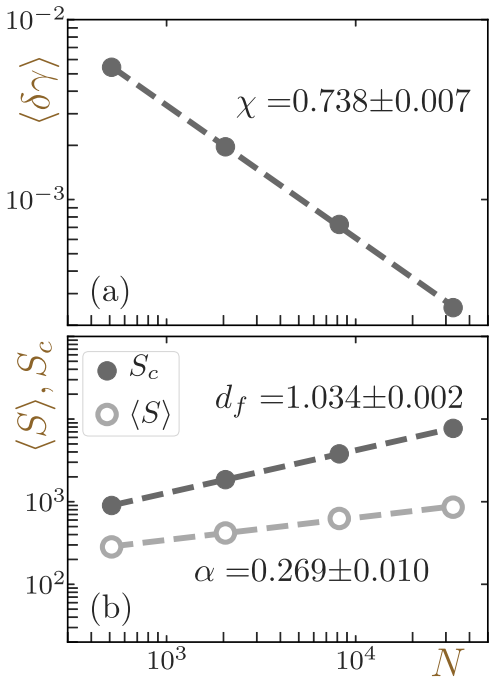

FIG. 2. The system size dependence of (a) the average strain interval between successive avalanches $\langle\delta\gamma\rangle$ and (b) the mean and cutoff avalanche sizes, $\langle S\rangle$ and S_c, in the steady state. The markers represent the numerical results, and the dashed lines are power-law fittings. The values of the exponents estimated from the fittings are also shown (with error).

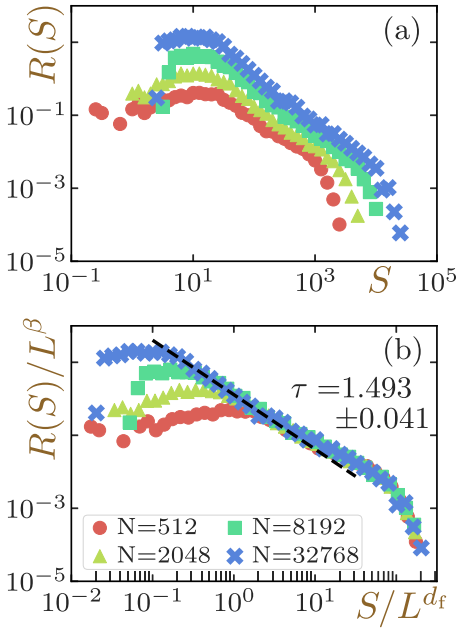

FIG. 3. Unit strain probability distribution of avalanche sizes $R(S)$ in the steady state (a) without scaling; (b) with finite-size scaling. The scaling exponents d_f and β are drawn from Table II. For both panels, different symbols are used for different system sizes, as shown in the legend in (b). The dashed line in (b) shows the power-law behavior predicted by the scaling law, Eq. (14), not a direct fitting result.

B. Avalanche size distribution

We now turn our attention to the avalanche size distribution. Figure 3(a) shows the results of the PDFs of the avalanche size per unit strain $R(S)$ for different system sizes. In Fig. 3(b) the same data are shown with a finite-size scaling with the exponents d_f and β. Here we demonstrate that the exponent β that is estimated solely from χ and d_f without any further fitting leads to a collapse of the results of different system sizes. This success of the collapse again supports the validity of our numerical calculation and the scaling laws.

We intuitively expect that the power-law behavior should appear in the large-size regime near the cutoff size S_c, and in fact, previous works have estimated the value of τ by a direct fitting of the data in that regime [47–50,52]. However, in Fig. 3(b) we see the power-law regime, $S^{-\tau}$ with $\tau \approx 1.493$, which the scaling relations suggest is located instead in the small-size regime. We would like to stress that this regime actually grows broader as the system size increases. This result suggests that the PDFs have peculiar bumps in the large-size regime; we now will reveal the origin of these bumps.

Before proceeding to the next section, we highlight that our value of $\tau \approx 1.493$ is much larger than the values reported in previous works with atomistic simulations [47–49]. In Appendix A 1, we show that if we estimate the value of τ in the same way as in previous works—namely, by a direct fitting of our data in the bumpy regime—we obtain $\tau \sim 1.19$. This value lies in the middle of those reported for the steady state in previous works, $\tau \in [1.15, 1.3]$. Based on this consistency, we believe that the values of τ in previous works varied widely only because the nonuniversal crossover regime was analyzed.

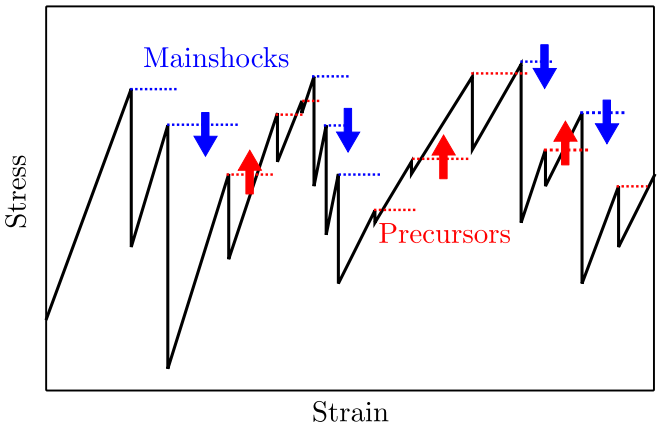

FIG. 4. Schematic of the definition of precursors and mainshocks. They are defined based on the relation between the stress just before the event of interest and the next one. The black lines depict the schematic stress-strain curve. The dotted lines compare the stresses immediately before successive events. The blue lines do not cross the stress-strain curve or mean downhill mainshocks, while the red lines cross them and indicate uphill precursors.

C. Origin of the bump in the large-size regime

The bumpy nature of the PDF suggests that the scaling function has a salient bumpy shape, and the distribution is possibly composed of two qualitatively different contributions: scale-free power-law events and system size-dependent percolated events. We discovered qualitatively different groups of avalanche events that prove this hypothesis. As sketched in Fig. 4, the evolution of the macroscopic stress under the AQS shear exhibits qualitatively different stress drop events—namely, uphill events and downhill events. Whether an event of interest is uphill or downhill is judged according to the relation between the stress immediately before the event and that of the next one, $\sigma(\gamma_{Ci})$ and $\sigma(\gamma_{Ci+1})$. If $\sigma(\gamma_{Ci})$ is smaller (larger) than $\sigma(\gamma_{Ci+1})$, the event of interest is considered to be an uphill (downhill) event. We call uphill events precursors and downhill events mainshocks hereafter. Note that we define precursors and mainshocks without introducing any parameters. In Fig. 5 we show that the PDF of the avalanche sizes can be decomposed into contributions from only precursors and mainshocks.[3] The results show that the bump is purely composed of mainshocks and that the PDF of precursors obeys a standard power-law behavior with a specific cutoff size. This suggests that the PDF of mainshocks includes an excess of large system-spanning events due to the finite-size effects in addition to unbounded scale-free events that obey the same power-law PDF as the precursors: events that are expected to become gigantic if the system size is extremely large (e.g., in the thermodynamic limit) stop their growth at around $S \approx S_c$ when the system size is not large enough. This effect results in a greater frequency of finding events with $S \approx S_c$ compared to the original power-law distribution and, thus, a

[3]The same precursor-mainshock decomposition works for other system sizes, and the results are qualitatively the same. See Appendix B 1.

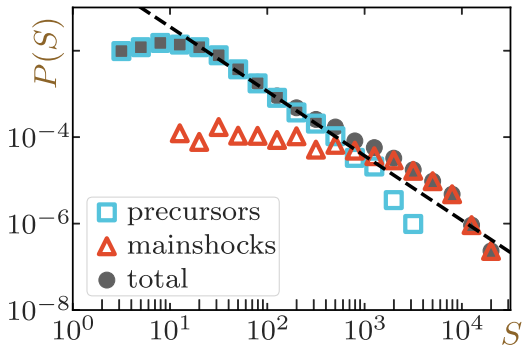

FIG. 5. Decomposition of the PDF of the avalanche sizes in the steady state into contributions from precursors and mainshocks. The PDFs of only precursors or mainshocks are normalized to the total number of events. The results for the system with $N = 32\,768$ are shown. The squares represent precursors, the triangles represent mainshocks, and the circles are the results of the total distribution, as shown in the legend. The dashed line is a power-law relation with the exponent shown in Fig. 3.

bump around $S \approx S_c$. Moreover, importantly, the ratio of the number of mainshocks to the total number of all avalanche events $p_{\rm main}$ decreases in a power-law manner as the system size increases (Fig. 6). Therefore, the statistics of avalanches in large systems are dominated by precursors (there is only a vanishing fraction of mainshocks that cannot contribute to the global shape of the PDF in the thermodynamic limit). This is additional supporting evidence that precursors are responsible for the intrinsic power-law behavior. We stress that, as is obvious from Fig. 5, mainshocks do not always possess large sizes (see also Appendix B 2 for more discussion on this issue). Also, we would like to emphasize again that to evaluate the critical exponents, we did not discard mainshocks. The dashed line shown in Fig. 5 represents the estimated results using Eq. (14) and χ and d_f that are determined by utilizing all events (including both precursors and mainshocks). Here, we provided an interpretation for the obtained value of τ. We stress that qualitatively similar bumpy PDFs have been reported in previous works [34,38,47–49,55,65,66], as discussed in detail below.

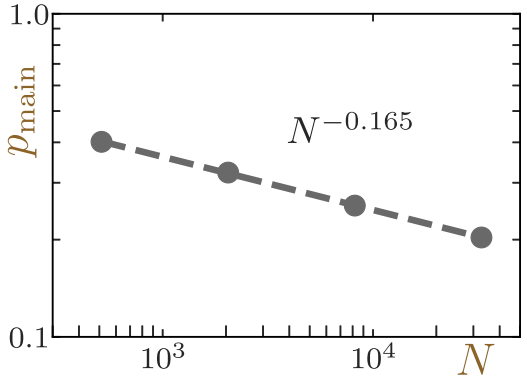

FIG. 6. The system size dependence of the fraction of mainshocks among events $p_{\rm main}$. The markers represent the numerical results, and the dashed line is a power-law fitting.

The direct visualization of the displacement field during a precursor and a mainshock provide more insight into the difference between the two event types (see Fig. 7). In particular, the events with the largest avalanche sizes for the same event types are shown. Here we highlight only mobile particles that are defined according to the participation ratio $e \equiv (\sum_i d_i^2)^2/(N \sum_i d_i^4)$, where $d_i = |\boldsymbol{d}_i|$ is the magnitude of the displacement vector of particle i. The participation ratio e provides the fraction of particles that are mobile: if all displacement vectors have the same magnitude, $e = 1$ holds, and if only one vector has a nonzero value, $e = 1/N$ holds. We define particles that have the e largest magnitudes of displacement vectors as mobile particles. As shown in Fig. 7, even in the largest event, the mobile particles of a precursor exhibit a localized structure, while the mainshock counterpart is system-spanning and is affected by the finite size of the system. Therefore, it is reasonable that precursors are mainly responsible for the intrinsic scale-free power-law regime. We stress that the event in Fig. 7(a) is a chain of multiple STZs.

The qualitative features of mainshocks that have been presented so far are reminiscent of the so-called runaway events observed in the MFD model [8,10]. In this model, such runaway events are expected only when *the weakening parameter* is positive—in other words, when the system shows brittle responses to an external shear, like metallic glasses. This may seem reasonable, since LJ glasses are sometimes used as a model system of metallic glasses [67]. However, our mainshocks exhibit qualitatively different scaling behavior from runaway events. In Ref. [68] it was reported that runaway events cannot be collapsed by the same scaling exponents as those for the power-law regime. In our case, on the other hand, entire PDFs can be collapsed by a single combination of scaling exponents, as presented in Fig. 3. In this sense, our mainshocks are qualitatively different from runaway events. It is also important to mention that several studies have reported that similar bumps in the PDFs of avalanche sizes can be induced by the inertial effect [47,48,65]. We emphasize that they seem to be different in nature from our mainshocks. This issue is discussed in detail in Appendix C. We would like to note that we are aware of qualitatively similar bumps in PDFs shown in previous works—in both experimental [38] and numerical works [34,49,55,66]. We emphasize that some of them are measured in completely inertialess conditions.

IV. EVOLUTION OF CRITICALITY IN THE ELASTIC REGIME

In this section the results in the elastic regime are presented. Specifically, to discuss the issues of criticality and universality independently, we separately present the results of the ensembles of only the initial avalanche events of different samples and of the avalanches collected over the entire elastic regime $\gamma \in [0, 0.02]$ [52].

A. Results for unperturbed systems

First, we present the results of the ensembles of only initial avalanche events, which should most strongly reflect the features of unperturbed systems. For each system size, we prepared 4000 independent samples and applied simple shear

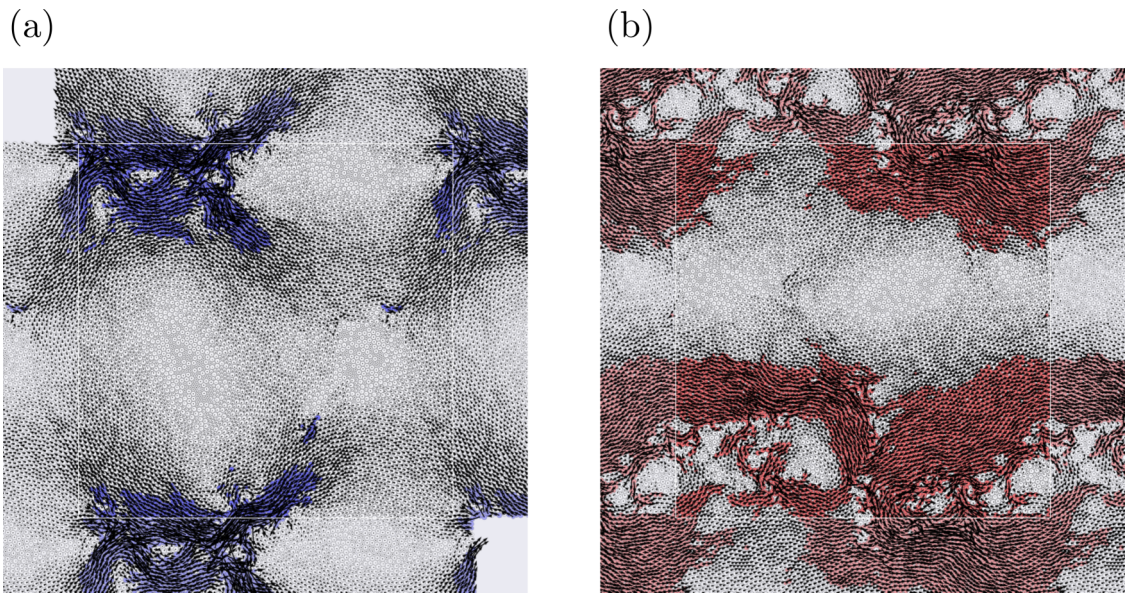

FIG. 7. Visualization of the displacement field during an avalanche event in a system with $N = 8192$: (a) precursor; (b) mainshock. Events with the largest avalanche sizes for the same event types are shown. The arrows represent the displacement vectors of particles and have been normalized properly for ease of viewing. The colored particles (shaded ones in gray scale) are mobile particles (see the main text for the definition). The copied cells due to the periodic boundary conditions are shown around the original cell with slightly lighter colors. White boxes represent the locations of the original cells.

in an AQS manner until we encountered avalanches. To judge whether the first obtained avalanche event was a precursor or a mainshock, we detected the first two events. The important statistical information is summarized in Fig. 8.

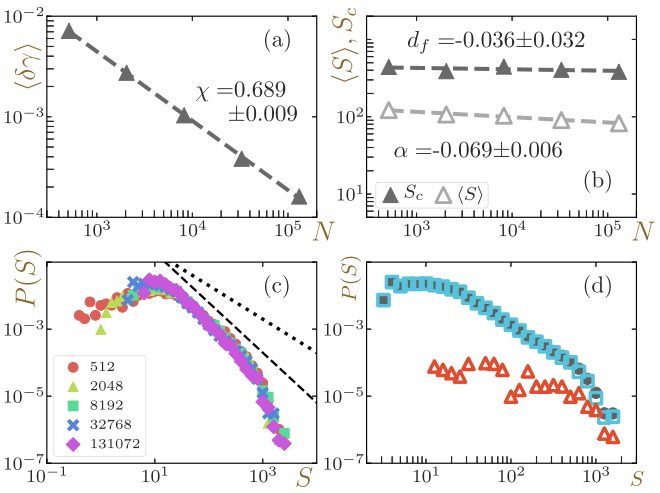

FIG. 8. Statistics of the first event ensemble. System size dependence of (a) $\langle\delta\gamma\rangle$, (b) $\langle S\rangle$ and S_c. The markers indicate the numerical results, and the lines are a power-law fitting. (c) PDFs of the avalanche sizes S. Different symbols are used for different system sizes, as shown in the legend. The dashed line depicts the results of power-law behavior with the exponent in the steady state, $\tau \approx 1.493$, and the dotted line denotes $\tau = 1.0$. (d) Decomposition of the PDF of the avalanche sizes of the first event ensemble into the contributions from precursors and mainshocks. The results for systems with $N = 32\,768$ are shown. The meanings of the markers are the same as in Fig. 5.

1. Independent exponents

The system size N dependence of $\langle\delta\gamma\rangle$ and S_c, which yield the independent exponents χ and d_f, is shown in Figs. 8(a) and 8(b). Although $\langle\delta\gamma\rangle$ exhibits power-law system size dependence, as in the steady state, S_c (and $\langle S\rangle$) appears rather constant (as characterized by very small negative exponents with large errors). This result is consistent with the findings reported in Ref. [32] and means that criticality is absent in unperturbed systems.

Note that Lin and coworkers have theoretically shown that the pseudogap exponent of an unperturbed system should be $\theta = 0.5$ universally [35]. This means that χ should be $2/3$, and our numerical result $\chi = 0.689$ is reasonably close to this theoretical prediction.

2. Avalanche size distribution

Since the statistics are system size-independent, the PDFs of the avalanche sizes of different system sizes are almost identical without any scaling [see Fig. 8(c)]. Interestingly, the PDFs still show broad power-law-like shapes. However, because of the absence of criticality, we cannot draw any absolute conclusion regarding whether they do indeed follow a power law, although their apparent *slopes* seem consistent with the value in the steady state, $\tau \approx 1.493$. Nevertheless, we can safely conclude that their apparent *slopes* are much larger than $\tau = 1.0$, which is the prediction of the theory in Ref. [60]. We also note that the PDFs do not exhibit bumps in the large-size regime, unlike the steady-state results.

3. Decomposition of avalanche size distribution

In Fig. 8(d) we demonstrate that the PDF of the first event ensemble can also be decomposed into contributions from the precursors and mainshocks. In this case, the mainshocks

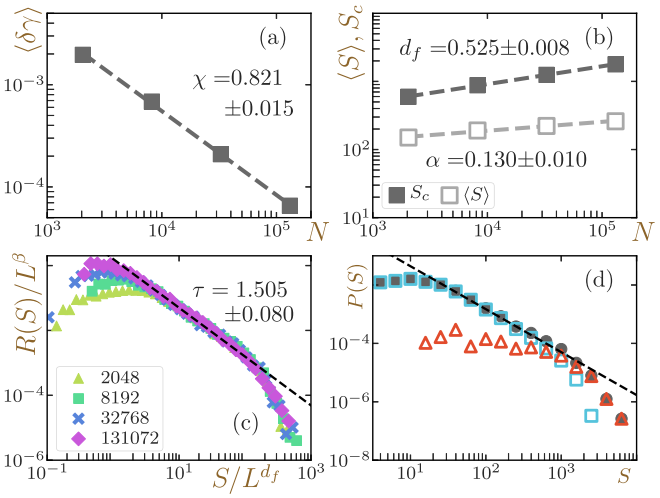

FIG. 9. Statistics of avalanches in the elastic regime $\gamma \in [0, 0.02]$. System size dependence of (a) $\langle\delta\gamma\rangle$, (b) $\langle S\rangle$ and S_c. The markers represent the numerical results, and the lines are the power-law fitting. (c) Scaled PDFs of the avalanche sizes S per unit strain. Different symbols are used for different system sizes, as shown in the legend. The dashed line indicates power-law behavior, with the exponent estimated by Eq. (17), $\tau \approx 1.505$. (d) Decomposition of the PDF of the avalanche sizes in the elastic regime into the contributions from precursors and mainshocks. The results for systems with $N = 32\,768$ are shown. The meanings of the markers are the same as in Fig. 5. The dashed line depicts the power-law behavior, with the exponent shown in Fig. 3.

are not well developed and are completely obscured by the precursors. This is why there are no bumps in the PDFs.

B. Results for weakly perturbed systems

We conduct the same analysis in the weakly perturbed elastic regime, $\gamma \in [0, 0.02]$ [52]. We performed simulations of 600, 160, 50, and 20 samples for systems with $N =$ 2048, 8192, 32 768, and 131 072, respectively. These sample numbers are chosen to guarantee more than 4000 events for each system size. The important statistical information is summarized in Fig. 9.

1. Independent exponents

In this case, all $\langle\delta\gamma\rangle$, $\langle S\rangle$, and S_c show power-law dependence on the system size N [see Figss. 9(a) and 9(b)]. The value of χ is larger than that in the steady state because of the well-known nonmonotonicity of the exponent χ, which was first predicted theoretically [35] and then numerically confirmed [50,52].[4] Nonzero values of α and d_f indicate criticality in the elastic regime, in accordance with Ref. [52]. However, the estimated values of χ and α do not meet Eq. (16), $\alpha = 1 - \chi$, since the stationarity condition (13) is trivially unsatisfied in this regime. We note that the same degree of discrepancy between α and $1 - \chi$ in the elastic regime was reported in Ref. [52].[5] We also mention that the fractal dimension d_f in the elastic regime is much less than that in the steady state.

2. Avalanche size distribution

The failure of Eq. (13) means that Eq. (14) is not applicable in this regime either.[6] However, by comparing Eq. (12) and the definition of the exponent α, we can derive another form of the scaling relation:

$$\tau = 2 - \alpha\frac{d}{d_f}. \tag{17}$$

This relation is robustly usable in the elastic regime. The estimation of τ with this new relation is $\tau \approx 1.505$, and it again describes the small-size regime of the PDFs of the avalanche sizes well [see Fig. 9(c)]. Moreover, we stress that this value is very close to the value in the steady state; thus, $\tau_{\mathrm{MFD}} = 1.5$. This result is in agreement with the experimental observations [40,42].

3. Decomposition of avalanche size distribution

The decomposition of the PDF of the avalanche sizes into the contribution from precursors and mainshocks again provides much information [Fig. 9(d)]. The PDF of the precursors shows normal power-law behavior with a cutoff, as is the case in the steady state, and moreover, the exponent seems to remain the same. In the elastic regime, unlike the case of the first event ensembles, the mainshocks form a small bump in the large-size regime.

Note that, as presented in Appendix A 2, since mainshocks come into play in this regime, we can fit the data in the crossover regime (which is close to the bump) directly by a power-law curve. The obtained value of the avalanche exponent τ' is quantitatively consistent with that in Ref. [52], $\tau' \approx 1.0$, where τ' is the avalanche exponent estimated by potential drops.

C. Unified view of avalanche criticality

All the results presented thus far provide a unified understanding of avalanche criticality and universality in the sheared LJ glass system throughout the whole strain regime. While the first event ensemble that represents the unperturbed system is off-critical, criticality emerges in both the elastic regime and the steady state. However, the fractal dimension of the avalanches indicates the quantitative difference between these two strain regimes. In particular, the elastic regime is described by a smaller value of d_f. In this sense, we conclude that criticality gradually grows as shear is applied and becomes fully developed in the steady state, where the fractal

[4] In Refs. [35,50,52], the so-called pseudogap exponent $\theta \equiv (1 - \chi)/\chi$ is investigated, instead of χ.

[5] This seems to have nothing to do with the fact that χ changes abruptly and nonmonotonically in the vicinity of $\gamma = 0$ because, even if we restrict ourselves to the strain range $\gamma \in [0.005, 0.02]$ in which χ temporarily becomes constant, as in Ref. [52], we observe the same results semiquantitatively.

[6] Equation (14) is expected to be valid even in the elastic regime if we conduct the measurement at a fixed stress level as in Ref. [62].

dimension is saturated. These observations are all consistent with previous works in the literature [31,52,62,69].

Once the system becomes critical, the avalanche critical exponent τ remains constant regardless of the amount of applied strain, and importantly, this value is consistent with the prediction by the MFD model [8], $\tau_{\rm MFD} = 1.5$. The universality of the exponent τ in the elastic regime is then at odds with the theoretical prediction made in Ref. [60]. This might be partly because the unperturbed system in our study is unlikely to be in the so-called Gardner phase [70–78],[7] while the theory in Ref. [60] assumed the Gardner nature of the unperturbed configurations. We repeatedly emphasize that the universal values of τ in each regime in our work are different from those in all previous numerical studies [47–52]. We consider that nonuniversal values in previous studies might have been obtained because the crossover regime resulting from the finite-size effects has been analyzed (see Appendix A).

Finally, we again stress that although the value of the critical exponent τ coincides with a famous mean-field value $\tau_{\rm MFD} = 1.5$ predicted in Ref. [8], this does not mean that this model succeeds in describing all features in sheared glasses. For example, it clearly fails, even qualitatively, to describe one aspect of the marginal stability of glasses, which is represented by the scaling relation $\langle \delta\gamma \rangle \sim N^{-\chi}$ with $0 < \chi < 1$.

V. CONCLUSION AND OVERVIEW

Here we conducted a thorough investigation of avalanche criticality in a sheared binary LJ glass system by means of atomistic simulations. In particular, by ruling out the ambiguity and arbitrariness that have slipped into measurements in previous studies, we first showed that the critical avalanche exponent τ in the steady state coincides with a mean-field prediction [8]. Our results simultaneously suggest that the scaling function of the avalanche size distribution has a nontrivial bumpy shape. We noticed that there are two qualitatively different avalanche events, and this binariness explains the physical origin of the strange bump in the scaling function. Furthermore, we demonstrated that this bump is likely to be the cause of the nonuniversal results for the critical exponent τ obtained in previous studies (Appendix A 1).

To investigate the change in criticality and universality due to applied shear, we conducted the same high-precision measurements of avalanche statistics of the first event ensemble, which reflect the properties of the unperturbed system and avalanches in the elastic regime. As a result, we confirmed that the first event ensemble does not exhibit any system size dependence and thus lacks criticality. This consequence dovetails with the result in Ref. [32]. Avalanches in the elastic regime, on the other hand, do display criticality, in accordance with Refs. [52,62], and again, the exponent of the power-law part is very close to a famous mean-field value $\tau_{\rm MFD} = 1.5$ universally. The value of the critical exponent is in accordance with recent experiments conducted in the elastic regime [40,42]. The criticality in the elastic regime is different from that in the steady state and is characterized by a much smaller value of the fractal dimension d_f. We believe that our results provide a unified picture of avalanche criticality in deformed glasses, for which confusing and seemingly conflicting results have been reported thus far: criticality itself develops along with applied strain, with the exponent of the power-law part remaining constant. In particular, the change in criticality is quantitatively encoded in the fractal dimension d_f, which takes the value of zero in the off-critical unperturbed state and saturates in the steady state.

We employed configurations that are not expected to be in the Gardner phase [73] as the initial state in this work, and thus, the starting point itself differs from the theory in Ref. [60], where a system in the Gardner phase is considered the initial state. If we find the Gardner phase in physical-dimensional amorphous solid systems with soft potentials, it would be very important and meaningful to conduct the same analyses using the configuration in the Gardner phase as the initial state.

Since we applied shear in an AQS way, dynamical information could not be accessed. In the future, conducting simulations with finite-rate shear and investigating dynamical information such as the avalanche duration, avalanche shape and power spectrum of the stress-drop rate time series would also be valuable.

ACKNOWLEDGMENTS

We thank Hajime Yoshino, Misaki Ozawa, and Harukuni Ikeda for enlightening discussions and Jean-Louis Barrat and Baoshuang Shang for useful comments on the manuscript. This work was financially supported by KAKENHI Grants (No. 18H05225, No. 19H01812, No. 19K14670, No. 20H01868, No. 20H00128, No. 20K14436, and No. 20J00802) and partially supported by the Asahi Glass Foundation.

APPENDIX A: COMPARISON WITH PREVIOUS WORKS

1. Avalanche exponent in the steady state

In this Appendix, we discuss the cause of the discrepancies between our result for the avalanche exponent $\tau \approx 1.493$ in the steady state and those in previous works with atomistic simulations, $1.15 \leqslant \tau \leqslant 1.3$ [47–49]. To this end, we measured τ by the same method as in the previous works: a direct fitting to the PDFs of avalanche sizes. In particular, we utilized only the data in the large-size regime, where the cutoff size S_c resides [the data points highlighted in gray in Fig. 10(a)]. As shown in Fig. 10(a), the resulting exponent $\tau = 1.19$ is located in the middle of the values reported in previous works. Thus, we consider that the cause of the variation in the value of τ might result from the fact that the nonuniversal part, which can depend on the details of the systems, has been fitted.

[7]Although several works have confirmed that the Gardner phase can be observed even in finite physical dimensions in hard sphere systems [72,74], at least thus far no work has detected the Gardner phase in a system with softer potentials, such as LJ or the inverse power law, in physical dimensions [73,75,76]. Thus, the Gardner nature in physical-dimensional glasses is currently a matter of very active debate [77].

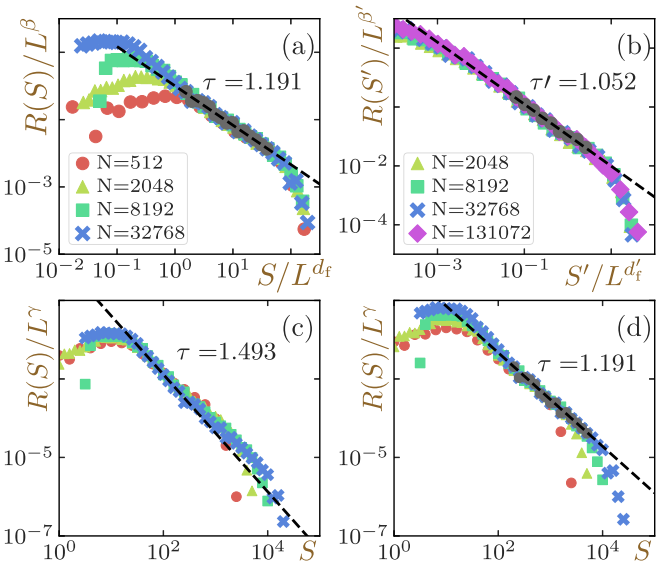

FIG. 10. (a) Scaled PDFs of the avalanche sizes defined based on the stress drops S in the steady state. (b) Scaled PDFs of the avalanche sizes defined based on the potential energy drops S' in the elastic regime. (c) Scaled PDFs of the avalanche sizes with the exponent γ estimated by $\tau = 1.493$, the value obtained in the main text. (d) Scaled PDFs of the avalanche sizes with the exponent γ estimated by $\tau = 1.19$, the value obtained in (a). In all panels, different symbols indicate different system sizes, as shown in the legends in (a) and (b). The dashed lines in (a), (b), and (d) depict the results of direct fitting by using the data points highlighted in gray. The estimated values of the avalanche exponents τ and τ' are also shown.

2. Avalanche exponent in the elastic regime

Although we used the stress drops for the definition of the avalanche sizes in the main text, the avalanche sizes can also be defined based on the potential energy drops, as follows:

$$S'_i \equiv \Delta E_{ABi} \equiv E_A(\gamma_{Ci}) - E_B(\gamma_{Ci}), \tag{A1}$$

where $E_s(\gamma)$ is the potential energy of state $s \in A, B$ at strain γ. We use the prime symbol to express the variables of the avalanches defined by Eq. (A1).

We also conducted the same direct fitting to the PDF of S', avalanche sizes defined based on the potential energy drops, in the elastic regime. The fitting result is $\tau' = 1.052$ and is perfectly consistent with the result in Ref. [52], as shown in Fig. 10(b).

3. Scaling collapse

We further demonstrate that the collapse of the data of different sizes by a scaling law is too robust, and thus, unfortunately, it is not reliable enough to guarantee the correctness of the results. In Refs. [47–49], the estimated value of τ is validated by the following scaling law:

$$\gamma = \beta + d_f \tau, \tag{A2}$$

where another scaling exponent γ[8] is introduced: by scaling by L^{γ}, the *power-law parts* of the PDFs of different system sizes can be collapsed, as shown in Fig. 10(c). Here, we estimated the value of γ by using only d_f and χ, as $\gamma = \beta + d_f\tau = d\chi$, as is the case for the other exponents. Note that the authors of Refs. [47–49] also confirmed that Eq. (11) holds for the obtained exponents.

What if we try the same scaling collapse with $\tau = 1.19$ that we obtained by the direct fitting to the data in Fig. 10(a)? The results are shown in Fig. 10(d) [in this case, we use Eq. (A2) to obtain the exponent γ]. As seen here, the *power-law parts* of different system sizes are collapsed again, even with a different value of τ. This means that Eq. (A2) can be satisfied, unexpectedly, too robustly with multiple values of τ, and the successful collapse by Eq. (A2) alone is not enough evidence for the validity of the obtained value of τ.

APPENDIX B: MEANING OF MAINSHOCKS

1. Decomposition of the avalanche size distribution in small systems

The decompositions of the PDF of avalanche sizes into contributions from precursors and mainshocks are valid for all system sizes. In Fig. 11 we show the results for systems with all $N = 512,\ 2048,\ 8192$, and 32 768 in the steady state. The qualitative results do not depend on the system size N: for all N, the contribution from precursors obeys a power law with the exponent obtained from the scaling law Eq. (14). Moreover, the contribution from the mainshocks seep through the small-size regime.

2. Mainshocks versus large events

In this section, we show that mainshocks are not merely identical to large events. We first define the fraction of large events by the following indicator $p_{>S_{\min}}$:

$$p_{>S_{\min}} \equiv \int_{S_{\min}}^{\infty} dSP(S), \tag{B1}$$

where $S_{\min}$ is a lower-bound threshold. This indicator $p_{>S_{\min}}$ gives the fraction of events that are larger than $S_{\min}$. In Fig. 12 we plot the results with several values of $S_{\min}$ as functions of N. As can be seen in this figure, $p_{>S_{\min}}$ is neither a power-law nor decreasing function regardless of the value of $S_{\min}$. This is at odds with p_{main}, which is a decreasing power-law function.

On the other hand, the cutoff avalanche size S_c grows with the system size N as $S_c \sim N^{d_f/d}$. Therefore, it may be more appropriate to employ a system-size-dependent threshold to ensure a fair comparison between mainshocks and large events. Thus, to estimate the fraction of events with $S \gtrsim S_c(N)$, we also measure the following indicator:

$$p_{S_c} \equiv \int_{aS_c}^{\infty} dSP(S), \tag{B2}$$

[8] Although we already used the letter γ to refer to the applied strain, we name this exponent γ following the definition of the original papers [47] to avoid any confusion.

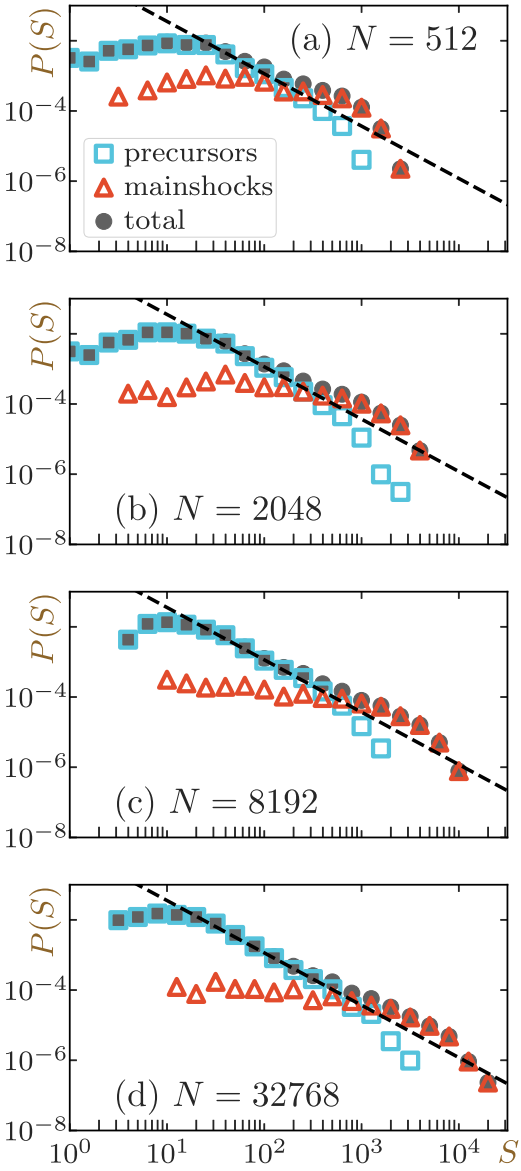

FIG. 11. Decomposition of the PDF of the avalanche sizes in the steady state into contributions from precursors and mainshocks. The PDFs of only precursors or mainshocks are normalized to the total number of events. The results for the systems with (a) $N = 512$, (b) $N = 2048$, (c) $N = 8192$, and (d) $N = 32\,768$ are shown. The squares represent precursors, the triangles represent mainshocks, and the circles are the results of the total distribution, as shown in the legend. The dashed line is a power-law relation with the exponent shown in Fig. 3.

where we set $a = 0.9$ (we have confirmed that the results hardly depend on the choice of the value of a if $a \geqslant 0.9$). This indicator p_{S_c} provides an estimation of the fraction of the population in the bumpy regime. We plot the results in Fig. 13 as a function of N. This indicator p_{S_c} decreases with increasing N in a power-law manner and is qualitatively consistent with p_{main}. However, the obtained value of the exponent here is markedly larger than the one in Fig. 6, indicating that the system size dependence of p_{main} and p_{S_c} are clearly different. This difference comes from the fact that mainshocks include

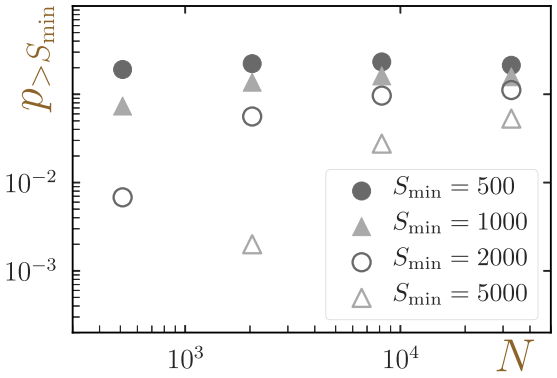

FIG. 12. The system size dependence of the fraction of large events that meet $S > S_{\min}$ to all events, $p_{>S_{\min}}$. Different symbols are used to distinguish the results with different values of $S_{\min}$ as shown in the legend.

small-size events. These results in Figs. 12 and 13 indicate that we cannot simply regard mainshocks as large events.

APPENDIX C: ARE MAINSHOCKS INDUCED BY THE INERTIAL EFFECT?

Several studies have reported that the introduction of inertia can induce bumps in the PDFs of avalanche sizes [47,48,65], which are similar to our mainshocks. We discuss the differences among our bumps and those of other studies.

In Ref. [65], Karimi and coworkers investigated the effect of inertia on the PDFs of avalanche sizes by numerical simulation of a finite-element-based elastoplastic model. They reported that as the effect of inertia becomes stronger, the PDF of the avalanche sizes begins to exhibit a characteristic bump in the large-size regime. Since we employed the FIRE algorithm in this work, which can introduce an inertial effect during the energy minimization process, it is possible that our mainshocks share the same origin as the bump reported in Ref. [65].

According to Karimi *et al.*, in the case of their elastoplastic model, the PDF of the minimum of the local stability $x_{\min}$ shows a bimodal nature when inertia takes effect, and the

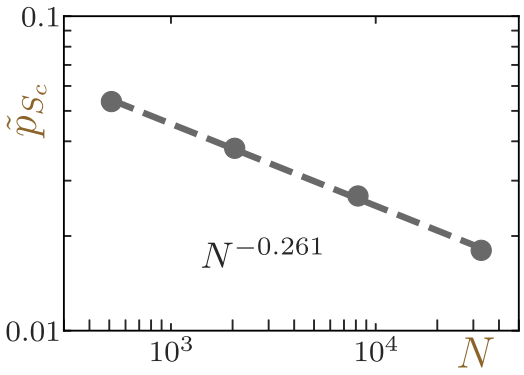

FIG. 13. The system size dependence of the fraction of events with $S \approx S_c$ to all events p_{S_c} in the steady state. For visualization, $\tilde{p}_{S_c} \equiv 0.5 p_{S_c}$ is shown. The markers represent the numerical results, and the dashed line is a power-law fitting.

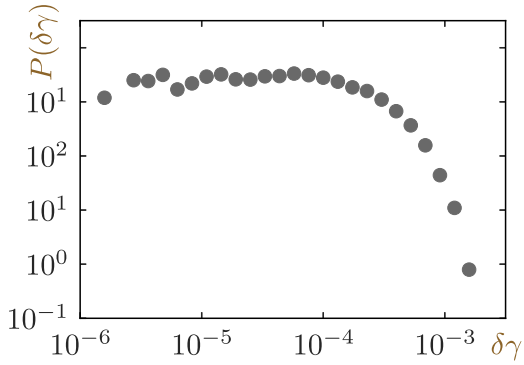

FIG. 14. PDF of $\delta\gamma$, or the local stability $x_{\min}$ in our setup. The steady-state result of a system with $N = 32\,768$ is shown.

peak in the large value of $x_{\min}$ is responsible for the bump in the PDF of the avalanche sizes. To check whether our bump has the same physical origin, we also measured the PDF of $\delta\gamma$, which represents the minimum of the local stability in our setup, as discussed in Sec. II D. As shown in Fig. 14, in our case, the PDF of $\delta\gamma$ does not exhibit any salient peaks in the large value regime. This means that the bump observed in our work has a qualitatively different physical origin from that in Ref. [65]. We note that the unimodal shape of $P(\delta\gamma)$ is consistent with Refs. [32,49].

Similar inertial effects have also been found in the atomistic simulations in Refs. [47,48]. Their results are qualitatively similar to those in our study (the bumps in their PDFs

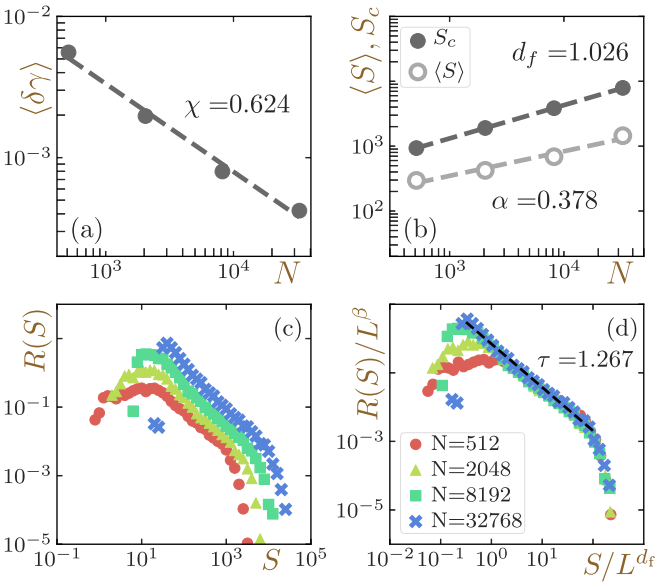

FIG. 15. Statistics of avalanches in the steady state with a fixed crude strain resolution of $\Delta\gamma = 1\times10^{-5}$. System size dependence of (a) $\langle\delta\gamma\rangle$, (b) $\langle S\rangle$ and S_c. The markers represent the numerical results, and the lines are the power-law fitting. (c) Unit strain PDFs of the avalanche size S. (d) Scaled unit strain PDFs of the avalanche size S. The dashed line in (d) depicts the power-law behavior predicted by the scaling law Eq. (14) with values of χ and d_f shown in (a), (b), $\tau \approx 1.276$. In both (c) and (d), different symbols indicate different system sizes, as shown in the legend in (d).

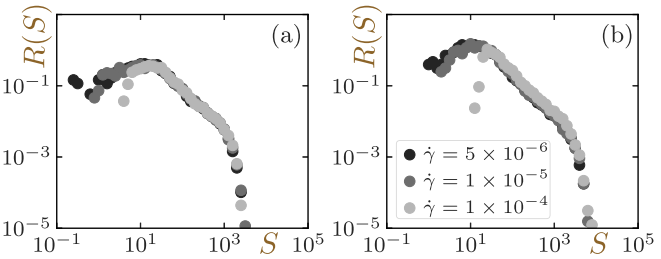

FIG. 16. Comparison of the PDFs of the avalanche sizes S with different strain resolutions $\Delta\gamma$. The results in the steady state are shown. (a) Results for $N = 512$ and (b) $N = 2048$. Different brightnesses represent different strain resolutions $\Delta\gamma$, as shown in the legend in (b).

exhibit the same scaling exponents as the ones for the power-law regime). However, the avalanche exponents obtained in the power-law regime are very different ($\tau = 1.0$ and 1.25 in their inertial cases). Therefore, we conclude that the bump in our scaling function is different from those in Refs. [47,48], and thus, our mainshocks are not due to the inertial effect possibly caused by the FIRE algorithm. Indeed, similar bumpy shapes have also been observed in studies where inertialess energy minimization protocols were employed [34,49,66].

APPENDIX D: VALIDATION OF STRAIN RESOLUTION

In this Appendix, we explain how the strain resolution $\Delta\gamma$ was determined. First, to provide intuition into the importance of the tuning of $\Delta\gamma$, we show the results with a fixed crude value of $\Delta\gamma = 1\times10^{-5}$ in Fig. 15. Here the statistical information in the steady state is shown. As shown in Figs. 15(a) and 15(b), the N dependence of $\langle\gamma\rangle$ and $\langle S\rangle$ obviously do not exhibit power-law shapes anymore (the clear deviation of the data of $N = 32\,768$ can be recognized). If we turn our attention to the PDF of the avalanche sizes [Fig. 15(c)], the data of the largest system size, $N = 32\,768$, do not reach the peak in the small-size regime due to the lack of resolution. If we still attempt to fit the N-dependence of $\langle\gamma\rangle$ and S_C to power-law curves and *estimate* the exponents χ, d_f and then τ from these data, we obtain $\tau \approx 1.267$. Note that, as shown in Fig. 15(d), this exponent does not seem to be inconsistent with the entire curve, and it is very difficult to tell that the result is incorrect if one looks only at the PDF of the avalanche sizes and not at the N dependence of $\langle\delta\gamma\rangle$. To summarize, the lack of resolution can lead to the deviation of the N dependence of $\langle\delta\gamma\rangle$ and $\langle S\rangle$ (and presumably S_c as well) from the expected power-law behavior. Moreover, the PDF of the avalanche sizes is truncated from the small-size regime where

TABLE III. Values of the strain resolution for different sets.

	$N = 512$	$N = 2048$	$N = 8192$	$N = 32\,768$
Set 1	5×10^{-6}	5×10^{-6}	5×10^{-6}	1×10^{-6}
Set 2	1×10^{-5}	1×10^{-5}	5×10^{-6}	1×10^{-6}
Set 3	5×10^{-6}	5×10^{-6}	5×10^{-6}	5×10^{-6}
Set 4	1×10^{-5}	1×10^{-5}	1×10^{-5}	1×10^{-5}

TABLE IV. Values of the critical exponents for different sets.

	τ	χ	d_f	α
Set 1	1.493	0.738	1.034	0.262
Set 2	1.493	0.743	1.013	0.259
Set 3	1.390	0.687	1.027	0.318
Set 4	1.267	0.624	1.026	0.378

the intrinsic power-law part resides. We carefully tuned the strain resolution $\Delta\gamma$ so that none of these problems appear.

We further note that to tune the resolution according to the procedure presented above, we need reliable data for small systems as a reference. For this purpose, we conducted simulations for small sizes, $N = 512,\ 2048$, with different resolutions, $\Delta\gamma = 1\times10^{-4},\ 1\times10^{-5},\ 5\times10^{-6}$ and confirmed that the PDF converges for $\Delta\gamma \leqslant 1\times10^{-5}$ (Fig. 16). This is why we employed the value $\Delta\gamma = 5\times10^{-6}$ for small systems.

The values of exponents obtained by different combinations of $\Delta\gamma$ are summarized in Table IV (the precise values of $\Delta\gamma$ for different values of N in different rows, which are denoted as "Set no.," are shown in Table III). From Table IV, it is noticeable that the $\Delta\gamma$ dependence is ruled out in our protocol (we have employed Set 1: there is only negligibly little difference between Sets 1 and *2*). More precisely, in the case of $N = 2048$, where the change in the dependence on $\Delta\gamma$ is significant within the range of $\Delta\gamma$ that we investigated, changing the resolution from $\Delta\gamma = 10^{-4}$ to $\Delta\gamma = 10^{-5}$ changes $\langle\gamma\rangle$ and $\langle S\rangle$ by more than 30%, while changing the resolution from $\Delta\gamma = 10^{-5}$ to $\Delta\gamma = 5\times10^{-6}$ changes them by less than 1% (see Table V).[9]

APPENDIX E: THE VALUE OF EXPONENT χ

The exponent χ, which is determined by the system size N dependence of the average interval between avalanches $\langle\delta\gamma\rangle$, is one important factor to discuss the avalanche criticality. There is a theoretical prediction for this exponent χ: Karmakar *et al.* [32] have theoretically shown that χ is expected to be $\chi = 2/3$ in the steady state, and the numerical results obtained with their MD simulation [20,31,32] and by another research group [47,48] [in these two articles, the authors did not show the values of χ explicitly: we utilized Eq. (16) to estimate χ] are consistent with this prediction. Moreover, several recent works with elastoplastic models have also reported consistent results [34,37,56,57]. On the other hand, in an article [49] reporting a thorough MD investigation, the values of χ are largely different from $\chi = 2/3$ (in Ref. [49], the authors considered two different potentials). If we estimate χ in Ref. [49] by using Eq. (16), results for two potentials are $\chi \approx 0.53$ and 0.49, respectively.[10] Therefore, a perfect consensus has not yet been formed regarding this exponent χ.

As we repeatedly stressed throughout the present article, however, we have found that, in MD simulations, the value of χ is largely dependent on the value of the strain resolution $\Delta\gamma$.[11] In such a situation, by definition, sufficiently small values of $\Delta\gamma$ at which the dependence on $\Delta\gamma$ is no longer present should be employed. We have used such values in this study (see Fig. 16 and Tables III and IV). Therefore, we consider that $\chi = 0.738$ is a reliable value obtained by a thorough numerical investigation. Note that to draw a conclusion for the universality of the value of χ (and thus other exponents such as τ), we must conduct similar investigation for other systems. We would like to leave this to future works.

APPENDIX F: COMPARISON OF VALUES OF CRITICAL EXPONENTS WITH PREVIOUS WORKS

In this Appendix, we provide a brief summary of measurement results of critical exponents of our own simulations and those from recent previous works in Table VI. Table VI contains results from all theoretical [8,32,35,56,60], numerical [34,48,49,52,56] and experimental [39,40,44] works. The exponent χ is calculated from Eq. (14) with the values of τ and d_f, if it is not available in the references.

APPENDIX G: COMPARISON WITH THE LINEAR CORRECTION METHOD

In the conventional linear correction method, the avalanche size is defined by Eq. (3). This definition includes ambiguity about the choice of the *shear modulus G*. We found that the results with this conventional linear correction method become quantitatively consistent with the rewinding method

[9]The value of S_c is basically determined by large-size events and does not depend much on $\Delta\gamma$ (accordingly, the value of d_f remains almost unchanged even when different values of $\Delta\gamma$ are employed: see Tables V, III, and IV).

[10]The authors of Ref. [49] introduced an exponent η whose definition is slightly different from that for χ and reported $\eta = 0.37$ and 0.49 for two potentials, respectively.

[11]We obtain a value of χ that is reasonably close to the theoretical prediction [32] and values of other existing numerical works [20,31,32,34,37,47,48,56,57], $\chi \approx 2/3$, if we employ Set 3: see Table IV.

TABLE V. $\Delta\gamma$ dependence of avalanche statistics for the system with $N = 2048$.

$\Delta\gamma$	1×10^{-4}	1×10^{-5}	5×10^{-6}
$\langle\delta\gamma\rangle$	0.00265 (34.5%)	0.00197	0.00196 (−0.5%)
$\langle S\rangle$	576 (36.2%)	423	420 (−0.7%)
S_c	1942 (2.0%)	1904	1846 (−3.0%)

Numbers in parentheses: the relative difference from the results with $\Delta\gamma = 1\times10^{-5}$.

TABLE VI. List of critical exponents obtained in previous works.

	τ	χ	d_f
	Theories		
Ref. [8] (MFD)	1.5	1	—
Ref. [32] (Bifurcation theory)	—	0.667	—
Ref. [35] (Mean-field theory[a])	—	0.667	—
Ref. [60] (Replica theory[a,b])	1.0	—	—
Ref. [56] (Mean-field theory)	—	0.667	—
	MD simulations		
Ref. [48][c]	1.3	0.685	0.9
Ref. [49][d]	1.25	0.53	1.25
Ref. [52][e]	1.0	0.667*	0.1–0.45
This work	1.493	0.738	1.034
	EPM simulations		
Ref. [34]	1.36	0.64	1.1
Ref. [56]	1.33	0.64	1.08
	Experiments		
Ref. [40][e]	1.5	—	—
Ref. [39][e]	1.24	—	—
Ref. [44]	1.3-1.7	—	—

[a]These results are for the first event ensemble.
[b]The result for systems above the jamming point.
[c]Only a part of the data from Ref. [48] is shown.
[d]Only a part of the data from Ref. [49] is shown.
[e]These results are for the elastic regime.

if we employ the following definition for the linear correction term:

$$G_i \Delta\gamma = [\sigma(\gamma_{Ci}) - \sigma(\gamma_{Ci} - \Delta\gamma)], \tag{G1}$$

where G_i is the shear modulus for the ith avalanche event and γ_{Ci} is the critical strain at which the ith avalanche event occurs. This definition is equivalent to a simple extrapolation of the last numerical step just before the event of interest is initiated. The measurement results of the critical exponents with linear correction with this definition are summarized in Table VII. The results are almost identical to those for the rewinding method (precursor or mainshock decomposition is also valid). To obtain the results in Table VII, we employed Set 1 as the strain resolution $\Delta\gamma$ (Table III).

TABLE VII. Values of the critical exponents obtained by the linear correction method.

τ	χ	d_f	α
1.486	0.739	1.015	0.254

[1] J. P. Sethna, K. A. Dahmen, and C. R. Myers, Crackling noise, Nature (London) **410**, 242 (2001).
[2] J. Faillettaz, F. Louchet, and J.-R. Grasso, Two-Threshold Model for Scaling Laws of Noninteracting Snow Avalanches, Phys. Rev. Lett. **93**, 208001 (2004).
[3] J. P. Sethna, K. Dahmen, S. Kartha, J. A. Krumhansl, B. W. Roberts, and J. D. Shore, Hysteresis and Hierarchies: Dynamics of Disorder-Driven First-Order Phase Transformations, Phys. Rev. Lett. **70**, 3347 (1993).
[4] K. Dahmen and J. P. Sethna, Hysteresis, avalanches, and disorder-induced critical scaling: A renormalization-group approach, Phys. Rev. B **53**, 14872 (1996).
[5] O. Narayan and D. S. Fisher, Threshold critical dynamics of driven interfaces in random media, Phys. Rev. B **48**, 7030 (1993).
[6] D. S. Fisher, Collective transport in random media: From superconductors to earthquakes, Phys. Rep. **301**, 113 (1998).
[7] M. Palassini and M. Goethe, Elementary excitations and avalanches in the Coulomb glass, J. Phys.: Conf. Ser. **376**, 012009 (2012).
[8] K. A. Dahmen, Y. Ben-Zion, and J. T. Uhl, Micromechanical Model for Deformation in Solids With Universal Predictions for Stress-Strain Curves and Slip Avalanches, Phys. Rev. Lett. **102**, 175501 (2009).
[9] D. S. Fisher, K. Dahmen, S. Ramanathan, and Y. Ben-Zion, Statistics of Earthquakes in Simple Models of Heterogeneous Faults, Phys. Rev. Lett. **78**, 4885 (1997).
[10] K. Dahmen, D. Ertaş, and Y. Ben-Zion, Gutenberg-Richter and characteristic earthquake behavior in simple mean-field models of heterogeneous faults, Phys. Rev. E **58**, 1494 (1998).
[11] M. A. Sheikh, R. L. Weaver, and K. A. Dahmen, Avalanche Statistics Identify Intrinsic Stellar Processes Near Criticality in KIC 8462852, Phys. Rev. Lett. **117**, 261101 (2016).

[12] R. V. Solé and S. C. Manrubia, Extinction and self-organized criticality in a model of large-scale evolution, Phys. Rev. E **54**, R42(R) (1996).

[13] L. de Arcangelis, C. Perrone-Capano, and H. J. Herrmann, Self-Organized Criticality Model for Brain Plasticity, Phys. Rev. Lett. **96**, 028107 (2006).

[14] N. Friedman, S. Ito, B. A. W. Brinkman, M. Shimono, R. E. Lee DeVille, K. A. Dahmen, J. M. Beggs, and T. C. Butler, Universal Critical Dynamics in High Resolution Neuronal Avalanche Data, Phys. Rev. Lett. **108**, 208102 (2012).

[15] S. Galam, Rational group decision making: A random field Ising model at $T = 0$, Physica A **238**, 66 (1997).

[16] C. Maloney and A. Lemaître, Universal Breakdown of Elasticity at the Onset of Material Failure, Phys. Rev. Lett. **93**, 195501 (2004).

[17] E. Aharonov and D. Sparks, Stick-slip motion in simulated granular layers, J. Geophys. Res. **109**, B09306 (2004).

[18] A. Tanguy, F. Leonforte, and J. L. Barrat, Plastic response of a 2D Lennard-Jones amorphous solid: Detailed analysis of the local rearrangements at very slow strain rate, Eur. Phys. J. E **20**, 355 (2006).

[19] N. P. Bailey, J. Schiøtz, A. Lemaître, and K. W. Jacobsen, Avalanche Size Scaling in Sheared Three-Dimensional Amorphous Solid, Phys. Rev. Lett. **98**, 095501 (2007).

[20] E. Lerner and I. Procaccia, Locality and nonlocality in elastoplastic responses of amorphous solids, Phys. Rev. E **79**, 066109 (2009).

[21] M. Tsamados, Plasticity and dynamical heterogeneity in driven glassy materials, Eur. Phys. J. E **32**, 165 (2010).

[22] C. Heussinger, L. Berthier, and J.-L. Barrat, Superdiffusive, heterogeneous, and collective particle motion near the fluid-solid transition in athermal disordered materials, Europhys. Lett. **90**, 20005 (2010).

[23] T. Hatano, C. Narteau, and P. Shebalin, Common dependence on stress for the statistics of granular avalanches and earthquakes, Sci. Rep. **5**, 12280 (2015).

[24] N. Oyama, H. Mizuno, and K. Saitoh, Avalanche Interpretation of the Power-Law Energy Spectrum in Three-Dimensional Dense Granular Flow, Phys. Rev. Lett. **122**, 188004 (2019).

[25] A. Abed Zadeh, J. Barés, and R. P. Behringer, Crackling to periodic dynamics in granular media, Phys. Rev. E **99**, 040901(R) (2019).

[26] M. L. Manning and A. J. Liu, Vibrational Modes Identify Soft Spots in a Sheared Disordered Packing, Phys. Rev. Lett. **107**, 108302 (2011).

[27] C. E. Maloney and A. Lemaître, Amorphous systems in athermal, quasistatic shear, Phys. Rev. E **74**, 016118 (2006).

[28] K. A. Dahmen, Y. Ben-Zion, and J. T. Uhl, A simple analytic theory for the statistics of avalanches in sheared granular materials, Nat. Phys. **7**, 554 (2011).

[29] M. Otsuki and H. Hayakawa, Avalanche contribution to shear modulus of granular materials, Phys. Rev. E **90**, 042202 (2014).

[30] G. Picard, A. Ajdari, F. Lequeux, and L. Bocquet, Elastic consequences of a single plastic event: A step towards the microscopic modeling of the flow of yield stress fluids, Eur. Phys. J. E **15**, 371 (2004).

[31] S. Karmakar, E. Lerner, I. Procaccia, and J. Zylberg, Statistical physics of elastoplastic steady states in amorphous solids: Finite temperatures and strain rates, Phys. Rev. E **82**, 031301 (2010).

[32] S. Karmakar, E. Lerner, and I. Procaccia, Statistical physics of the yielding transition in amorphous solids, Phys. Rev. E **82**, 055103(R) (2010).

[33] J. Lin, A. Saade, E. Lerner, A. Rosso, and M. Wyart, On the density of shear transformations in amorphous solids, Europhys. Lett. **105**, 26003 (2014).

[34] J. Lin, E. Lerner, A. Rosso, and M. Wyart, Scaling description of the yielding transition in soft amorphous solids at zero temperature, Proc. Natl. Acad. Sci. USA **111**, 14382 (2014).

[35] J. Lin and M. Wyart, Mean-Field Description of Plastic Flow in Amorphous Solids, Phys. Rev. X **6**, 011005 (2016).

[36] J. T. Parley, S. M. Fielding, and P. Sollich, Aging in a mean field elastoplastic model of amorphous solids, Phys. Fluids **32**, 127104 (2020).

[37] E. E. Ferrero and E. A. Jagla, Properties of the density of shear transformations in driven amorphous solids, J. Phys.: Condens. Matter **33**, 124001 (2021).

[38] B. A. Sun, H. B. Yu, W. Jiao, H. Y. Bai, D. Q. Zhao, and W. H. Wang, Plasticity of Ductile Metallic Glasses: A Self-Organized Critical State, Phys. Rev. Lett. **105**, 035501 (2010).

[39] J. Barés, D. Wang, D. Wang, T. Bertrand, C. S. O'Hern, and R. P. Behringer, Local and global avalanches in a two-dimensional sheared granular medium, Phys. Rev. E **96**, 052902 (2017).

[40] J. Antonaglia, W. J. Wright, X. Gu, R. R. Byer, T. C. Hufnagel, M. LeBlanc, J. T. Uhl, and K. A. Dahmen, Bulk Metallic Glasses Deform Via Slip Avalanches, Phys. Rev. Lett. **112**, 155501 (2014).

[41] J. T. Uhl, S. Pathak, D. Schorlemmer, X. Liu, R. Swindeman, B. A. W. Brinkman, M. LeBlanc, G. Tsekenis, N. Friedman, R. Behringer, D. Denisov, P. Schall, X. Gu, W. J. Wright, T. Hufnagel, A. Jennings, J. R. Greer, P. K. Liaw, T. Becker, G. Dresen, and K. A. Dahmen, Universal quake statistics: From compressed nanocrystals to earthquakes, Sci. Rep. **5**, 16493 (2015).

[42] D. V. Denisov, K. A. Lörincz, J. T. Uhl, K. A. Dahmen, and P. Schall, Universality of slip avalanches in flowing granular matter, Nat. Commun. **7**, 10641 (2016).

[43] X. Tong, G. Wang, J. Yi, J. L. Ren, S. Pauly, Y. L. Gao, Q. J. Zhai, N. Mattern, K. A. Dahmen, P. K. Liaw, and J. Eckert, Shear avalanches in plastic deformation of a metallic glass composite, Int. J. Plast. **77**, 141 (2016).

[44] K. A. Murphy, K. A. Dahmen, and H. M. Jaeger, Transforming Mesoscale Granular Plasticity through Particle Shape, Phys. Rev. X **9**, 011014 (2019).

[45] M. LeBlanc, A. Nawano, W. J. Wright, X. Gu, J. T. Uhl, and K. A. Dahmen, Avalanche statistics from data with low time resolution, Phys. Rev. E **94**, 052135 (2016).

[46] K. Maeda and S. Takeuchi, Computer simulation of deformation in two-dimensional amorphous structures, Phys. Status Solidi **49**, 685 (1978).

[47] K. M. Salerno, C. E. Maloney, and M. O. Robbins, Avalanches in Strained Amorphous Solids: Does Inertia Destroy Critical Behavior? Phys. Rev. Lett. **109**, 105703 (2012).

[48] K. M. Salerno and M. O. Robbins, Effect of inertia on sheared disordered solids: Critical scaling of avalanches in two and three dimensions, Phys. Rev. E **88**, 062206 (2013).

[49] D. Zhang, K. A. Dahmen, and M. Ostoja-Starzewski, Scaling of slip avalanches in sheared amorphous materials based on large-scale atomistic simulations, Phys. Rev. E **95**, 032902 (2017).

[50] M. Ozawa, L. Berthier, G. Biroli, A. Rosso, and G. Tarjus, Random critical point separates brittle and ductile yielding transitions in amorphous materials, Proc. Natl. Acad. Sci. USA **115**, 6656 (2018).
[51] K. Saitoh, N. Oyama, F. Ogushi, and S. Luding, Transition rates for slip-avalanches in soft athermal disks under quasi-static simple shear deformations, Soft Matter **15**, 3487 (2019).
[52] B. Shang, P. Guan, and J. L. Barrat, Elastic avalanches reveal marginal behavior in amorphous solids, Proc. Natl. Acad. Sci. USA **117**, 86 (2020).
[53] M. Talamali, V. Petäjä, D. Vandembroucq, and S. Roux, Avalanches, precursors, and finite-size fluctuations in a mesoscopic model of amorphous plasticity, Phys. Rev. E **84**, 016115 (2011).
[54] Z. Budrikis and S. Zapperi, Avalanche localization and crossover scaling in amorphous plasticity, Phys. Rev. E **88**, 062403 (2013).
[55] Z. Budrikis, D. F. Castellanos, S. Sandfeld, M. Zaiser, and S. Zapperi, Universal features of amorphous plasticity, Nat. Commun. **8**, 15928 (2017).
[56] E. E. Ferrero and E. A. Jagla, Criticality in elastoplastic models of amorphous solids with stress-dependent yielding rates, Soft Matter **15**, 9041 (2019).
[57] E. E. Ferrero and E. A. Jagla, Elastic Interfaces on Disordered Substrates: From Mean-Field Depinning to Yielding, Phys. Rev. Lett. **123**, 218002 (2019).
[58] C. Liu, E. E. Ferrero, F. Puosi, J.-L. Barrat, and K. Martens, Driving Rate Dependence of Avalanche Statistics and Shapes at the Yielding Transition, Phys. Rev. Lett. **116**, 065501 (2016).
[59] P. Leishangthem, A. D. S. Parmar, and S. Sastry, The yielding transition in amorphous solids under oscillatory shear deformation, Nat. Commun. **8**, 14653 (2017).
[60] S. Franz and S. Spigler, Mean-field avalanches in jammed spheres, Phys. Rev. E **95**, 022139 (2017).
[61] C. Ruscher and J. Rottler, Residual stress distributions in amorphous solids from atomistic simulations, Soft Matter **16**, 8940 (2020).
[62] J. Lin, T. Gueudré, A. Rosso, and M. Wyart, Criticality in the Approach to Failure in Amorphous Solids, Phys. Rev. Lett. **115**, 168001 (2015).
[63] M. P. Allen and D. J. Tildesley, *Computer Simulation of Liquids* (Oxford University Press, Oxford, 1987).
[64] E. Bitzek, P. Koskinen, F. Gähler, M. Moseler, and P. Gumbsch, Structural Relaxation Made Simple, Phys. Rev. Lett. **97**, 170201 (2006).
[65] K. Karimi, E. E. Ferrero, and J.-L. Barrat, Inertia and universality of avalanche statistics: The case of slowly deformed amorphous solids, Phys. Rev. E **95**, 013003 (2017).
[66] E. Lerner, N. P. Bailey, and J. C. Dyre, Density scaling and quasiuniversality of flow-event statistics for athermal plastic flows, Phys. Rev. E **90**, 052304 (2014).
[67] W. Kob and H. C. Andersen, Testing mode-coupling theory for a supercooled binary Lennard-Jones mixture. II. Intermediate scattering function and dynamic susceptibility, Phys. Rev. E **52**, 4134 (1995).
[68] J. M. Carlson, J. S. Langer, B. E. Shaw, and C. Tang, Intrinsic properties of a Burridge-Knopoff model of an earthquake fault, Phys. Rev. A **44**, 884 (1991).
[69] G. Parisi, I. Procaccia, C. Rainone, and M. Singh, Shear bands as manifestation of a criticality in yielding amorphous solids, Proc. Natl. Acad. Sci. USA **114**, 5577 (2017).
[70] P. Charbonneau, J. Kurchan, G. Parisi, P. Urbani, and F. Zamponi, Fractal free energy landscapes in structural glasses, Nat. Commun. **5**, 3725 (2014).
[71] P. Charbonneau, Y. Jin, G. Parisi, C. Rainone, B. Seoane, and F. Zamponi, Numerical detection of the Gardner transition in a mean-field glass former, Phys. Rev. E **92**, 012316 (2015).
[72] L. Berthier, P. Charbonneau, Y. Jin, G. Parisi, B. Seoane, and F. Zamponi, Growing timescales and lengthscales characterizing vibrations of amorphous solids, Proc. Natl. Acad. Sci. USA **113**, 8397 (2016).
[73] C. Scalliet, L. Berthier, and F. Zamponi, Absence of Marginal Stability in a Structural Glass, Phys. Rev. Lett. **119**, 205501 (2017).
[74] Y. Jin, P. Urbani, F. Zamponi, and H. Yoshino, A stability-reversibility map unifies elasticity, plasticity, yielding, and jamming in hard sphere glasses, Sci. Adv. **4**, eaat6387 (2018).
[75] C. L. Hicks, M. J. Wheatley, M. J. Godfrey, and M. A. Moore, Gardner Transition in Physical Dimensions, Phys. Rev. Lett. **120**, 225501 (2018).
[76] B. Seoane, D. R. Reid, J. J. de Pablo, and F. Zamponi, Low-temperature anomalies of a vapor deposited glass, Phys. Rev. Mater. **2**, 015602 (2018).
[77] L. Berthier, G. Biroli, P. Charbonneau, E. I. Corwin, S. Franz, and F. Zamponi, Gardner physics in amorphous solids and beyond, J. Chem. Phys. **151**, 010901 (2019).
[78] G. Parisi, P. Urbani, and F. Zamponi, *Theory of Simple Glasses* (Cambridge University Press, Cambridge, 2020).